Radiative cooling of an Al plasma in an AlTi mixture heated by an ultraintense laser pulse

P. Renaudin, L Duthoit, S. Baton, Ch Blancard, A. Chaleil, P Cossé, G Faussurier, L. Gremillet, L. Lecherbourg, B. Loupias, et al.

Radiative cooling of an Al plasma in an AlTi mixture heated by an ultraintense laser pulse

P. Renaudin[a,*], L. Duthoit[a,b], S. Baton[b], Ch. Blancard[a], A. Chaleil[a], P. Cossé[a], G. Faussurier[a], L. Gremillet[a], L. Lecherbourg[a,c], B. Loupias[a], F. Perez[b]

[a] *CEA, DAM, DIF, F-91297 Arpajon, France*
[b] *LULI, CNRS, Ecole Polytechnique, 91120 Palaiseau, France*
[c] *LOA, ENSTA ParisTech, CNRS, Ecole Polytechnique, Univ. Paris-Saclay, 91120 Palaiseau, France*

Abstract

The rapid heating and cooling dynamics of thin solid foils driven by an ultraintense ($\sim 10^{18}$ Wcm^{-2}) picosecond laser pulse has been experimentally studied through time-integrated and time-resolved x-ray emission spectroscopy as well as 2D x-ray imaging. Targets consisted of plastic foils with buried Al or $Al_{42}Ti_{58}$ layers, with Al as a tracer to infer the plasma conditions. Our measurements indicate that the Al K-shell emission occurs over a shorter duration and from a narrower region in AlTi mixtures compared to pure Al samples. The experimental data are consistent with a simple model describing the fast heating and expansion of the foil target, and pinpoint the importance of radiative cooling in high-Z samples.

Keywords: x-ray spectroscopy, Non-LTE kinetics, Radiative cooling

1. Introduction

Radiative cooling plays a major role in inertial confinement fusion [1], magnetic confinement fusion [2], and laser-produced plasmas [3]. The plasma cooling function is also an important property in many astrophysics settings, including highly collimated jets [4], star formation [5], or the interstellar medium [6]. Radiative effects are strongly dependent on the atomic number (Z) of the medium considered. Laser-based plasma experiments on radiative collapse relevant to astrophysical jets have thus shown that high-Z (Fe or Au) jets are narrow and collimated, whereas lower-Z (CH or Al) plasma jets were much broader [7]. However, no direct evidence of the enhanced cooling of low-Z, multicharged ions within a low-Z/high-Z mixture has been provided yet. Such measurements would help advance our understanding of nonlocal thermodynamic equilibrium (NLTE) radiative processes, which may critically affect the thermodynamic and energy transport properties of high-energy-density plasmas (HEDPs) [8]. As of now, the lack of experimental data under such conditions hampers the validation of NLTE atomic models in HEDPs [9], and so there is a pressing need for highly resolved, laser-based experiments under well-controlled conditions.

In past two decades, ultraintense ($> 10^{18}$ Wcm^{-2}), short-pulse ($\sim 0.1 - 1$ ps) lasers have proven to be efficient tools to generate hot ($\gtrsim 0.1$ keV) plasmas at near-solid density [10, 11, 12, 13, 14, 15, 16, 17, 18, 19]. In related experiments, the plasma heating results from the rapid slowdown of the MeV-range nonthermal electrons generated at the irradiated target side. The current density of those fast electrons is usually high enough that, besides direct collisions with target particles, the dominant heating process is the ohmic dissipation of the inductive return current formed by collisional background (thermal) electrons [20, 21, 22]. While many works aimed at characterizing and modeling the fast heating dynamics of thin ($\sim \mu$m) targets irradiated by ultraintense laser pulses, the associated radiative cooling mechanisms remain little addressed [23, 24].

This paper reports on experimental measurements of the heating (and cooling) of a metallic layer buried in a plastic foil driven by an ultraintense picosecond laser pulse. In order to isolate the effect of radiative losses under otherwise similar conditions, we varied the composition of the buried layer (or "sample"), employing either Al or $Al_{42}Ti_{58}$, where Al served as a spectroscopic

*Corresponding author
Email address: patrick.renaudin@cea.fr (P. Renaudin)

tracer. The experimental Al K-shell emission was found to be shorter in time, and to originate from a smaller region, when Ti was mixed with Al. The variation in the x-ray emission duration is consistent with a detailed analysis of the Al K-shell spectra, based on a reduced model for the target heating and relaxation dynamics. This agreement suggests that the observed narrower x-ray emissive region in AlTi mixtures mainly originates from enhanced radiative losses.

2. Experimental setup

The experiment was performed using the LULI2000 laser system, which delivered a frequency-doubled pulse of 0.527 μm wavelength, 1.3 ps FWHM duration and 15 J energy. It was focused to a 14 μm FHWM spot size (deduced from the 156 ± 15 μm^2 area of the focal spot measured at low fluence), yielding an on-target intensity of a few 10^{18} Wcm^{-2} (assuming 20 % of the laser energy was contained within the first lobe). Despite frequency doubling, a residual prepulse of intensity 6×10^{-6} times that of the main pulse was measured.

The targets, irradiated at a 25° angle from the surface normal, were 500 μm wide, square-shaped, three-layer foils. They were composed of 2 μm C_8H_8/0.2 μm X/2 μm C_8H_8, where the buried layer X (or "sample") was either made of Al or $Al_{42}Ti_{58}$. The areal mass of the targets was measured through Rutherford backscattering at CEA, from which the solid density of the $Al_{42}Ti_{58}$ layer was deduced (ρ = 4.2 g/cm^3).

The first diagnostic was a space- and time-integrated von Hamos x-ray spectrometer (henceforth referred to as VH) placed at ~ 48° from the rear surface normal. It consisted of a pentaerythritol (PET) cylindrically bent crystal designed to record the Al K-shell spectra from the $1s^2 - 1s2p$ (He$_\alpha$) to the $1s - 3p$ (Ly$_\beta$) lines onto an image plate (IP) detector with a 2.2 eV spectral resolution.

In addition, a time-resolved x-ray spectrometer (referred to as PolyX) placed along the front surface normal measured the temporal evolution of some of the Al K-shell lines (Ly$_\alpha$ and He$_\beta$). It comprised a curved cesium hydrophthalate (CsAP) crystal coupled to a picosecond streak camera, so as to produce time-resolved spectra with a 2 ps resolution [25]. The on-axis x-ray emission was first collected and collimated by a matrix of hollow glass capillaries, which ensured a high collection angle and transmission over a broad spectral range (~ 1 – 10 keV) [26]. X rays were transported a few tens of cm and focused onto the 15 mm long, 100 μm wide entrance slit of the streak camera. This allowed the hard x-ray emission level to be reduced at the entrance slit of the streak camera, and thus the signal-to-noise ratio to be optimized.

Finally, a two-channel, high-resolution x-ray imager (FUHRI [27]) was designed to record the He$_\beta$ line in the spectral range 1850 ± 50 eV and the Ly$_\beta$ line in the spectral range 2050 ± 50 eV, with a resolution of 2.7 ± 0.3 μm. It was made of two Fresnel phase zone plates fabricated from the same substrate, and located 26 cm away from the plasma, each associated with one multilayer mirror for spectral selection [28]. Both images were recorded by one CCD camera. The spatial resolution was measured at the PTB synchrotron radiation facility and at the CEA EQUINOX laser facility [29].

3. Experimental results

The measured Al K-shell spectra in Fig. 1 show lines from He-like and H-like Al ions that mainly depend on the achieved density and temperature. In the temperature range explored in the experiment, the ratio of the area under the He$_\beta$ line profile to that under the Ly$_\beta$ line (called *line ratio* thereafter) is very sensitive to the electron temperature. The plasma is optically thin for these two lines. Note that the number of Al atoms decreases from pure Al to $Al_{42}Ti_{58}$ samples, reducing the signal-to-noise ratio on the IP. Nevertheless, line ratios are similar in both plasmas, suggesting that they have been heated up to similar maximum electron temperatures ($T_{e,\max}$).

Figure 2 displays typical FUHRI images of the x-ray emissive regions in the pure Al plasma, in the He$_\beta$ (left)

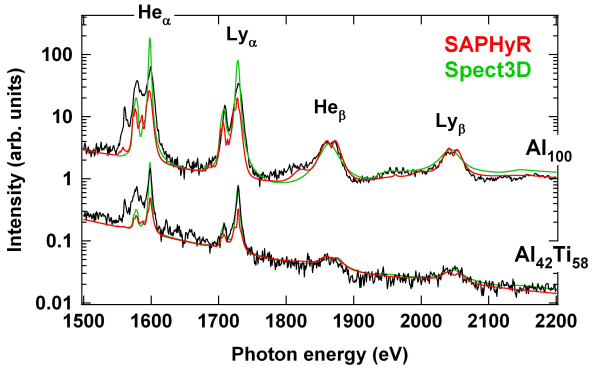

Figure 1: Time-integrated Al K-shell spectra recorded with the VH spectrometer (averaged over 7 Al shots and 3 $Al_{42}Ti_{58}$ shots), compared with spectra from two different models (see text). Spectra from the pure Al layer were artificially shifted by a factor of 10 for clarity.

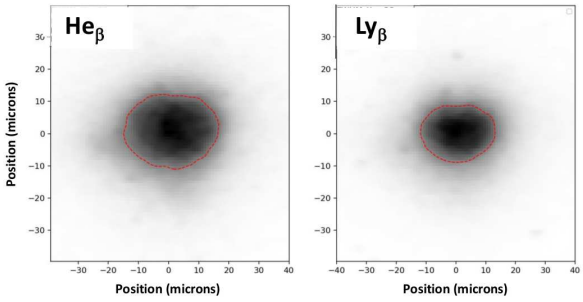

Figure 2: Images of the He_β (left) and Ly_β (right) line emission sources from a pure Al sample, as recorded by the FUHRI diagnostic. Red curves plot the half-maximum intensity contours.

	Al	$Al_{42}Ti_{58}$
He_β	1210 ± 180	880 ± 130
Ly_β	660 ± 100	610 ± 90

Table 1: Areas (in μm^2) of the Al He_β and Ly_β emissive zones, averaged over 8 Al and 3 $Al_{42}Ti_{58}$ shots.

and Ly_β (right) spectral ranges. The emission spot size of the Ly_β line appears to be smaller than that of the He_β line, an expected result since the former corresponds to a higher ionization state of the Al plasma. Table 1 gathers the measured values of the emissive areas (delimited by the half-maximum intensity contours and averaged over a few shots). Note that those values largely exceed the $156 \pm 15\,\mu m^2$ laser spot area as measured at low fluence. The Al He_β line emission spot shrinks significantly in the AlTi mixture. This trend is less pronounced for the Ly_β line emission. This indicates that the hotter central region, which mainly accounts for the Ly_β radiation, has a similar size in both cases, but also that the moderately heated region associated with the He_β radiation is wider in Al than in $Al_{42}Ti_{58}$.

Figure 3 presents the time evolution of the Al Ly_β line emission from the Al and $Al_{42}Ti_{58}$ samples, as measured by the PolyX diagnostic. Both the Al Ly_α and He_β lines from the Al plasma were measured with this diagnostic, but it was not possible to record the He_β line with a sufficient signal-to-noise ratio in the $Al_{42}Ti_{58}$ case. The measured FWHM durations of the Ly_α and He_β line emissions are summarized in Table 2. The Ly_α line emission appears to be shorter in $Al_{42}Ti_{58}$, indicative of a faster recombination caused by a larger electron density and enhanced radiative cooling.

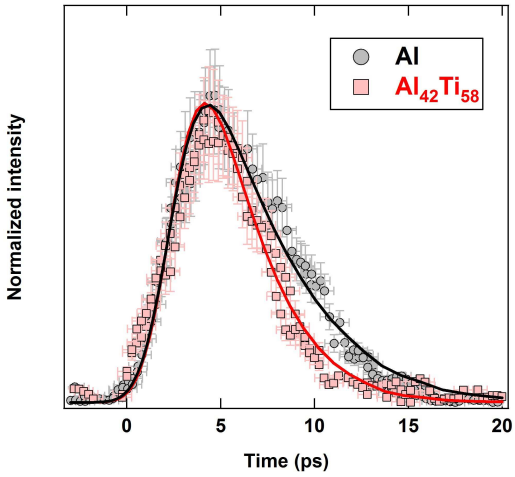

Figure 3: Temporal evolution of the Al Ly_α emission measured with PolyX. The black and red lines plot the results of the model coupled to SPECT3D (see text).

	Al	$Al_{42}Ti_{58}$
He_β	8.1 ± 0.1	-
Ly_α	9.7 ± 1.8	6.9 ± 0.5

Table 2: FWHM duration (in ps) of the Al He_β and Ly_α emission measured with PolyX (averaged over 8 Al shots and 3 $Al_{42}Ti_{58}$ shots).

4. Modeling of the plasma emission dynamics

The most accurate description of the ultrafast dynamics of solid-density plasmas subject to intense laser pulses is nowadays provided by particle-in-cell (PIC) kinetic simulation codes, enriched with collisional and atomic physics models [17, 30, 31, 32]. Yet, due to their computational cost, such simulations remain difficult to perform in multidimensional geometries over the multi-picosecond time scales relevant to our measurements.

As a much simpler alternative, we have turned to a semi-analytical 0D model [33] in order to reproduce the measured time-integrated x-ray spectra and their temporal dynamics. This model describes the heating and expansion of a uniformly heated, thin plasma slab induced by a dilute hot-electron population. The 0D assumption is justified by the laser spot size and the hot-electron deceleration length being much larger than the target thickness. This model was proposed and detailed in Ref. [33], where it was shown to provide a satisfactory match to optical interferometric measurements of the dynamics of laser-driven foil targets. In the following, we will only recall its main features.

The relaxation of the hot electrons (subscript h)

through the target is solved using a multi-group approach, assuming an initial energy distribution of the form $f_h(E) \propto \exp(-E/k_B T_{h0})$ between $E_{\min} = 10\,\mathrm{keV}$ and $E_{\max} = 10T_{h0}$. This distribution is decomposed into $N = 100$ groups, each having a numerical weight given by $p_i = \exp(-E_{hi}/T_{h0})/\sum_{i=1}^{N}\exp(-E_{hi}/k_B T_{h0})$. The energy equations obeyed by the ith hot-electron group and the bulk electrons (subscript e) and ions (subscript i) are:

$$\frac{dE_{hi}}{dt} = \frac{L_e(t)}{L_h(t)}\Pi(E_{hi}, n_e, Z^*)v_{hi} - \frac{L_e(t)}{L_h(t)}\frac{\eta(T_e)j_h^2}{n_h} + \left.\frac{dE_{hi}}{dt}\right|_{\mathrm{ad}}, \quad (1)$$

$$C_e(T_e)\frac{dT_e}{dt} = n_h\sum_{i=1}^{N} p_i\Pi(E_{hi}, n_e, Z^*)v_{hi} - Q_r + \eta(T_e)j_h^2/C_e - G_{ei}(T_e - T_i) + C_e\left.\frac{dT_e}{dt}\right|_{\mathrm{ad}}, \quad (2)$$

$$C_i(T_i)\frac{dT_i}{dt} = G_{ei}(T_e - T_i) + C_i\left.\frac{dT_i}{dt}\right|_{\mathrm{ad}}. \quad (3)$$

We have introduced v_{hi} the velocity of the ith hot-electron group, $\Pi(E_{hi}, n_e, Z^*)$ the stopping power due to bound and free (bulk) electrons as well as to plasmons [34], n_h and j_h the number and current densities of the fast electrons, n_e the bulk electron density, Z^* the ionization degree [35], and η the electrical resistivity [36]. $L_h(t)$ and $L_e(t)$ denote the longitudinal extents of the hot and bulk populations, which are assumed to expand self-similarly [37]. In the two-temperature model of the bulk target, C_e and C_i are the electron [38] and ion [39] heat capacities, and G_{ei} is the electron-ion coupling parameter [33]. The radiated power density is expressed as $Q_r \equiv f_r Q_B Q_{BB}/(Q_B + Q_{BB})$, where Q_B and Q_{BB} represent, respectively, the Bremsstrahlung and the black-body radiation [40], and f_r is an adjustment factor. The terms $dE_{hi}/dt|_{\mathrm{ad}}$, $dT_e/dt|_{\mathrm{ad}}$, and $dT_i/dt|_{\mathrm{ad}}$ describe the adiabatic cooling of the hot electrons and bulk populations during their expansion. In Eq. (1) the factor L_e/L_h in the stopping power and resistive terms measures the reduction in the energy transfer due to the hot electrons' expanding on a distance (L_h) larger than the bulk target size (L_e). The right-hand term in Eq. (1) accounts for the slowing down induced by the resistive field $E \sim \eta j_h$. Once the hot electrons start recirculating through the target, we expect their net current and the associated resistive heating to drop significantly. In practice, j_h is thus assumed to vanish for times larger than the average transit time of the hot electrons through the target.

The system dynamics, which is solved numerically, is therefore uniquely governed by the input (*initial*) parameters T_{h0}, n_{h0}, T_{e0}, and T_{i0}. Thermal equilibrium at room temperature is initially assumed for the bulk target ($T_{e0} = T_{i0} = 300\,\mathrm{K}$). The initial hot-electron temperature, is estimated from Beg's law [41], $T_{h0}[\mathrm{keV}] \simeq 215\,(I_0\lambda_0^2/10^{18}\,\mathrm{Wcm^{-2}}\,\mu\mathrm{m}^2)^{1/2}$. In those calculations, the maximum foil temperature, $T_{e,\max}$, can be considered as a variable parameter, controlled by the initial fast-electron density, n_{h0}, to obtain the best agreement with the time-integrated VH spectra. Moreover, we have adjusted the radiative loss factor, f_r, so as to best reproduce the time-resolved PolyX data.

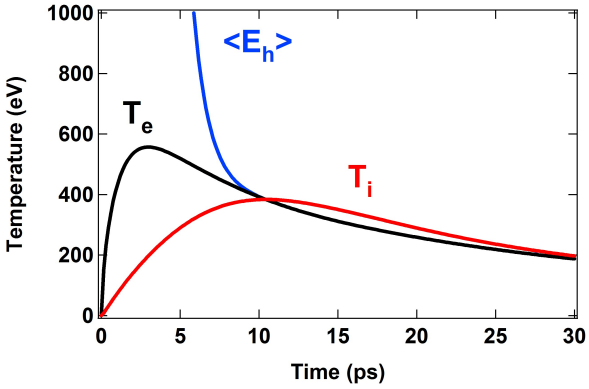

Figure 4: Evolution of the plasma temperatures in Al as predicted by the model with $\langle E_h\rangle = 150\,\mathrm{keV}$, $n_{h0} = 4.1\times10^{21}\,\mathrm{cm^{-3}}$, and $f_r = 2.5$.

As a typical example, Fig. 4 presents the temporal evolution of the average hot-electron energy, $\langle E_h\rangle$, and of the plasma temperatures, as predicted by the model for $T_{h0} = 150\,\mathrm{keV}$, $n_{h0} = 4.1\times10^{21}\,\mathrm{cm^{-3}}$, and $f_r = 2.5$. The relaxation of the average hot-electron energy takes about $\sim 10\,\mathrm{ps}$, whereas the bulk-electron temperature reaches a maximum of $\simeq 550\,\mathrm{eV}$ in $\sim 3\,\mathrm{ps}$.

The temporal evolution of the K-shell emission has been computed by post-processing the model's output with two different atomic physics codes. The first one, SPECT3D, generates NLTE spectra using a time-dependent collisional-radiative model [42]. The second one, SAPHYR, developped at CEA, uses a stationary collisional-radiative model. Figure 1 shows a comparison between the VH data and the time-integrated x-ray spectra calculated using the same parameters as in Fig. 4. The model appears to reproduce accurately the line ratio in both Al and $Al_{42}Ti_{58}$, but does not capture well the absolute He_α and Ly_α intensities. This is especially true for the pure Al plasma. Transverse temperature gradients, quantified in Tab. 1, could explain such a discrepancy. The agreement is better in $Al_{42}Ti_{58}$, where the similar sizes of the Ly_β and He_β emissive zones

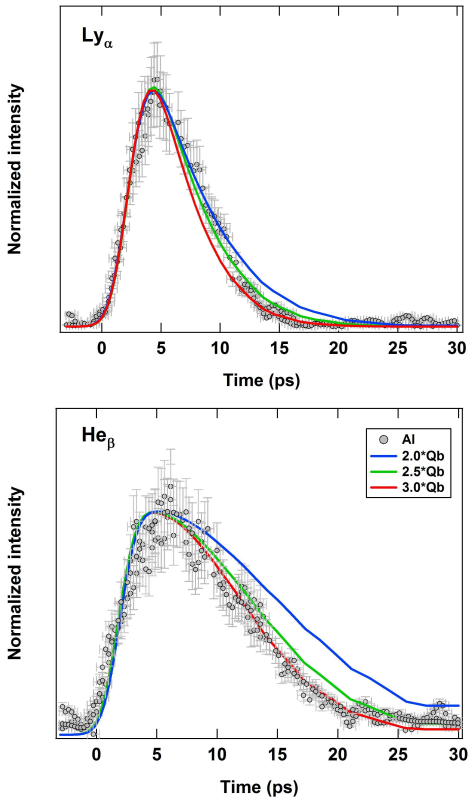

Figure 5: Temporal evolution of the Al Ly$_\alpha$ (spectral integration between 1720 and 1740 eV) and He$_\beta$ (spectral integration between 1855 and 1885 eV), as measured with PolyX. The results of the model coupled to SPECT3D are given for different values of the radiative loss factor f_r (see text).

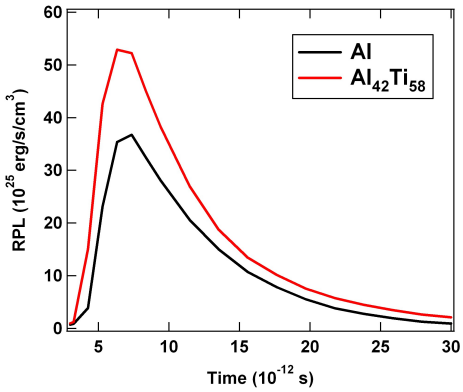

Figure 6: Radiative power loss (RPL) of Al and $Al_{42}Ti_{58}$ plasmas along the thermodynamic path displayed in Fig. 4 and calculated by the SAPHYR model.

suggest reduced 2D effects. The line ratio observed in $Al_{42}Ti_{58}$ suggests that the same $T_{e,\max}$ is reached than in Al, despite variations in the target properties. As already pointed out in Ref. [33], $T_{e,\max}$ is much more sensitive to n_{h0} than to T_{h0}, and so only a slight increase in n_{h0} to 5.4×10^{21} cm^{-3} is needed to yield $T_{e,\max} \simeq 550$ eV in $Al_{42}Ti_{58}$.

The temporal profiles of the Al He$_\beta$ and Ly$_\alpha$ lines measured by PolyX are compared to the model coupled with SPECT3D in Fig. 5, for different values of f_r. The best agreement is obtained for $f_r \simeq 2.5 \pm 0.5$. The two lines have different temporal durations, the He$_\beta$ line lasting the longest. This feature is well reproduced by the model, the He$_\beta$ line being less affected by radiative losses than the Ly$_\alpha$ line due to the "freezing" of collisional recombination in expanding and cooling He-like plasmas [43]. Repeating this analysis for the $Al_{42}Ti_{58}$ plasma gives the same best-fitting value for f_r. Figure 3 compares the measured and synthetic time evolutions of the Ly$_\alpha$ line, for Al and $Al_{42}Ti_{58}$ ($f_r = 2.5$ in both cases). The overall good agreement between the data and the model is further proof that the increased radiative losses in $Al_{42}Ti_{58}$ (at $T_e = 500$ eV, Q_r is ~1.5 times larger than in Al) are the main cause for the shortened Ly$_\alpha$ line emission.

It is well known [7] that the importance of radiative losses is determined by the ratio of the radiative cooling time, $\tau_{\rm rad} = 1.5 n_e k_B (T_e + T_i/Z^*)/Q_r$, to the hydrodynamic time, $\tau_{\rm hyd} \simeq D/c_s$, where D is the size of the emissive region and c_s is the sound speed. Regardless of the target composition, and taking for D the results from Tab. 2, we find that $\tau_{\rm hyd} \simeq 100$ ps for a solid-density plasma at $T_e = 500$ eV. For a more accurate estimate of $\tau_{\rm rad}$, the SAPHYR code was used to compute the cooling rate of the Al and $Al_{42}Ti_{58}$ plasmas along the thermodynamic paths predicted by the model (see Fig. 6). This yielded a value of ~ 3 ps for $\tau_{\rm rad}$. Therefore, whatever the plasma composition, it appears that (i) the plasma is radiatively cooled, and that (ii) radiative cooling mainly occurs at early times, around the maximum of T_e. This is the reason for the reduction in the x-ray emission area in $Al_{42}Ti_{58}$ plasmas. In a follow-up study, two-dimensional radiative-hydrodynamic simulations will be performed to provide a better insight into the radiation-modified dynamics of the heated foil targets.

5. Conclusions

In summary, by isolating the effects of radiation under otherwise similar experimental conditions (changing the atomic number of the target), and measuring the

x-ray emission with high spatial ($\sim 3\,\mu$m) and temporal (~ 2 ps) resolution, we have characterized the impact of the radiative flux on the Al K-shell emission from multilayer targets heated by an ultraintense laser pulse. The enhanced radiative cooling in $Al_{42}Ti_{58}$ plasmas compared to pure Al entail a x-ray emission both shorter in time and narrower in space. The experimental data are correctly captured by a simple model, showing a decreasing x-ray duration with increasing atomic number. This study opens a method to measure the radiative cooling rates in HEDPs and to benchmark simulations of NLTE radiative processes in hot dense plasmas.

Acknowledgments

We thank the LULI2000 technical team for their day-to-day support as well as the CEA Valduc team for performing the RBS measurements.

References

[1] J. D. Lindl et *al*., Phys. Plasmas **2**, 3933 (1995).
[2] M. Bitter et *al*., Phys. Rev. Lett. **71**, 1007 (1993).
[3] B. Qing et *al*., Appl. Phys. Lett. **110**, 084103 (2017).
[4] J. M. Stone and M. L. Norman, Astrophys. J. **413**, 198 (1993).
[5] B. Reipurth and J. Bally, Annu. Rev. Astron. Astrophys. **39**, 403 (2001).
[6] Y. Wang et *al*., MNRAS **440**, 3100 (2014).
[7] K. Shigemori et *al*., Phys. Rev. E **62**, 8838 (2000).
[8] W. J. Gray et *al*., Phys. Plasmas **25**, 062702 (2018).
[9] R. Piron et *al*., HEDP **23**, 38 (2017).
[10] K. Nazir et *al*., Appl. Phys. Lett. **69**, 3686 (1996).
[11] A. Saemann et *al*., Phys. Rev. Lett. **82**, 4843 (1999).
[12] R. G. Evans et *al*., Appl. Phys. Lett. **86**, 191505 (2005).
[13] D. J. Hoarty et *al*., HEDP. **3**, 115 (2007).
[14] J. J. Santos et *al*., Phys. Plasmas **14** 103107, (2007); New J. Phys. **19**, 103105 (2017).
[15] S. N. Chen et *al*., Phys. Plasmas **16**, 062701 (2009).
[16] P. M. Nilson et *al*., Phys. Rev. E **79**, 016406 (2009).
[17] F. Perez et *al*., Phys. Rev. Lett. **104**, 085001 (2010).
[18] C. R. D. Brown et *al*., Phys. Rev. Lett. **106**, 185003 (2011).
[19] V. Dervieux et *al*., HEDP **16**, 12 (2015).
[20] A. R. Bell and R. J. Kingham, Phys. Rev. Lett. **91**, 035003 (2003).
[21] A. P. L. Robinson et *al*., Nucl. Fusion **54**, 054003 (2014).
[22] L. G. Huang et *al.*, Phys. Plasmas **23**, 063112 (2016).
[23] R. Shepherd et *al*., J. Quant. Spectrosc. Radiat. Transfer **58**, 911 (1997).
[24] P. Audebert et *al*., J. Quant. Spectrosc. Radiat. Transfer **81**, 19 (2003).
[25] C. Reverdin et *al*., Proc. of Science, EPs Conf. on Plasma Diagnostics 2015, 042 (2015).
[26] F. Dorchies, N. Fedorov, and L. Lecherbourg, Rev. Sci. Instrum. **86**, 073106 (2015).
[27] A. Do et *al*., Rev. Sci. Instrum. **88**, 013701 (2017).
[28] A. Do et *al*., Rev. Sci. Instrum. **89**, 113702 (2018).
[29] C. Reverdin et *al*., Rev. Sci. Instrum. **79**, 10E932 (2008).
[30] R. Mishra et *al*., Phys. Plasmas **20**, 072704 (2013).
[31] L. G. Huang et *al*., Phys. Plasmas **24**, 103115 (2017).
[32] D. Wu et *al*., High Power Laser Sci. Eng. **6**, e50 (2018).
[33] P. Antici et *al*., Phys. Plasmas **20**, 123116 (2013).
[34] V. V. Val'Chuk, N. B. Volkov, and P. A. Yalovets, Plasma Phys. Rep. **21**, 159 (1995).
[35] R. M. More., *Atomic and Molecular Physics of Controlled Thermonuclear Fusion*, edited by C. J. Joachain and D. E. Post (Plenum Publishing Corporation, 1983), pp. 399–439.
[36] Y. T. Lee and R. M. More, Phys. Fluids B **27**, 1273 (1984).
[37] D. S. Dorozhkina and V. E. Semenov, Phys. Rev. Lett. **81**, 2681 (1998).
[38] D. Fisher et *al*., Phys. Rev. E **65**, 016409 (2001).
[39] R. M. More et *al*, Phys. Fluids B **31**, 3059 (1988).
[40] S. Atzeni, Phys. Plasmas **6**, 3316 (1999).
[41] F. N. Beg et *al*., Phys. Plasmas **4**, 447 (1997).
[42] J. MacFarlane et *al*., HEDP **3**, 181 (2007).
[43] A. Klisnick et *al*., Phys. Rev. E **53**, 5315 (1996).